Fluid-Structure Interaction Modeling of the Aortic Hemodynamics in Adult Zebrafish: a Pilot Study based on Synchrotron X-Ray Tomography

Matthias Van Impe, Lisa Caboor, Violette Deleeuw, Margie Olbinado, Julie De Backer, Patrick Sips, Patrick Segers

***Abstract*—*Objective:* The zebrafish is increasingly used as a small animal model for cardiovascular disease, including vascular disorders. Nevertheless, a comprehensive biomechanical understanding of the zebrafish cardiovascular circulation is still lacking and possibilities for phenotyping the zebrafish heart and vasculature at adult – no longer optically transparent – stages are limited. To improve these aspects, we developed imaging-based 3D models of the cardiovascular system of wild-type adult zebrafish. *Methods: In vivo* high-frequency echocardiography and *ex vivo* synchrotron x-ray tomography were combined to build fluid-structure interaction finite element models of the fluid dynamics and biomechanics inside the ventral aorta. *Results:* We successfully generated a reference model of the circulation in adult zebrafish. The dorsal side of the most proximal branching region was found as the location of highest first principal wall stress and was also a location of low wall shear stress. Reynolds number and oscillatory shear were very low compared to mice and humans. *Significance:* The presented wild-type results provide a first extensive biomechanical reference for adult zebrafish. This framework can be used for advanced cardiovascular phenotyping of adult genetically engineered zebrafish models of cardiovascular disease, showing disruptions of the normal mechano-biology and homeostasis. By providing reference values for key biomechanical stimuli (including wall shear stress and first principal stress) in wild-type animals, and a pipeline for image-based animal-specific computational biomechanical models, this study contributes to a more comprehensive understanding of the role of altered biomechanics and hemodynamics in heritable cardiovascular pathologies.**

***Index Terms*—adult zebrafish; animal model for cardiovascular disease; aortic hemodynamics; wall shear stress; synchrotron x-ray tomography; fluid-structure interaction modeling**

I. Introduction

ZEBRAFISH (Danio rerio) emerged as a powerful animal model to study the pathophysiological mechanisms leading to human disease, including cardiovascular disorders [1]-[3]. For over two decades now, the use of this small vertebrate as a model for cardiovascular disease has continued to gain interest. Genetic tractability, ease of maintenance, cost-efficiency and potential for high-throughput applications provide unique advantages to zebrafish over mammalian animal models, including mice. Despite major anatomical differences, many aspects of human cardiovascular development, genetics and molecular mechanisms are conserved. Zebrafish are well suited to complement mammalian animal models as an effective and versatile screening tool, particularly for heritable conditions [4] and pharmacological research [5], [6].

The development [7] and regeneration [8] of the heart (ventricle) have received considerable attention, but zebrafish can also be used as a model for aortic disease [9]-[15]. Zebrafish models show potential to provide a better understanding of the basic underlying pathological mechanisms in heritable thoracic aortic disease, a crucial aspect that remains elusive despite available mouse models. A complete description of (the progression of) heritable thoracic aortic disease in zebrafish requires the study of early as well as adult stages. The optical transparency of zebrafish embryos and larvae, in combination with the availability of fluorescent reporters in transgenic lines, allows efficient *in vivo* visualization of the developing cardiovascular structures [16], [17]. Technological innovations such as CRISPR/Cas9 to generate genetically modified lines [18] and light sheet fluorescence microscopy for fast high-resolution three-dimensional imaging [19], [20] have boosted research on both cardiovascular development and early stage cardiovascular phenotyping. Optical transparency however is lost in adult zebrafish and *in vivo* imaging options at adult stages become more limited. The transparent *casper* mutant zebrafish strain allows (limited) microscopic observation of more superficially located internal tissue structure at adult stages [21], [22], but imaging of the deeper located ventral and

This paragraph of the first footnote will contain the date on which you submitted your paper for review. This work was supported in part by an interdisciplinary research grant of the Ghent University special research fund (IOP038-18) and in part by the Baillet-Latour Grant for Medical Research awarded to Julie De Backer. *(Corresponding author: Matthias Van Impe.)*

Matthias Van Impe and Patrick Segers are with IBiTech-bioMMeda, Ghent University, 9000 Gent, Belgium (e-mail: matthias.vanimpe@ugent.be).

Lisa Caboor, Violette Deleeuw and Patrick Sips are with the Department of Biomolecular Medicine, Ghent University.

Margie Olbinado is with the Swiss Light Source, Paul Scherrer Institut.

Julie De Backer is with the Department of Biomolecular Medicine, Ghent University and the Department of Cardiology, University Hospital Ghent.

dorsal aorta is not possible *in vivo*. At this point, high-frequency echocardiography is the most common state-of-the-art technique to characterize cardiovascular function in adult zebrafish [23]-[26].

Phenotyping of cardiovascular structure and function extends beyond anatomical imaging, and should also address biomechanical factors as indicators of aortic disease and as intrinsic components of the mechano-biological environment within which pathophysiological processes take place. Especially wall shear stress (WSS), i.e., the shear stress exerted by the blood flow on the endothelial cells that line the vessel wall, and the stress/stretch inside the vessel wall are key metrics [27]-[29]. Including biomechanical aspects is crucial for a comprehensive understanding of (defects in) the zebrafish cardiovascular system since the biomechanical and mechano-biological role may be equally important as the biological functions. The first studies on cardiovascular biomechanics in zebrafish focused on the heart and described the embryonic ventricular fluid dynamics [30]-[37]. So far, little is known about the biomechanical aspects of the aorta in zebrafish. Different techniques such as micro particle image velocimetry, confocal microscopy and light-sheet fluorescence microscopy can be used to describe blood flow and wall shear stress in the circulation of developing zebrafish. Both in the work of Lee *et al.* [38] and in the follow-up study by Choi *et al.* [39] an equivalent circuit model of the caudal microvasculature was used to investigate the link between atherosclerosis and low WSS. Very recently, Roustaei *et al.* [40] also focused on the (caudal) microvasculature and investigated the effect of tail amputation and regeneration by using 4D computational fluid dynamics (CFD). The novel zebrafish models of aortic disease will most likely direct biomechanical research in developing zebrafish to the proximal circulation as well. However, information on the cardiovascular fluid dynamics and biomechanics in adult zebrafish is completely lacking. Nonetheless, describing the aortic biomechanics in adult zebrafish would be valuable to validate hypotheses generated at developmental stages and to study progressive or late-onset conditions. In this study, we have modeled the fluid dynamics and biomechanics of the ventral aorta of adult zebrafish.

Thus far, investigation of the cardiovascular structure in adult zebrafish has mostly relied on standard histochemical techniques [41], [42]. Through sectioning, detailed *ex vivo* observations are possible, but for finite element modeling, other imaging techniques that effectively integrate three-dimensional cardiovascular information are more suited. Synchrotron x-ray micro-computed tomography (synchrotron micro-CT or synchrotron imaging) has already been successfully applied in zebrafish but until now only very limited results on (cardiovascular) soft tissue details, especially at adult stages, were reported [43]-[46]. We applied synchrotron imaging in adult wild-type zebrafish, and combined the synchrotron-based 3D reconstructions of the aorta with *in vivo* high-frequency echocardiography measurements to set up both computational fluid dynamics (CFD) and fluid-structure interaction (FSI) finite element models. This framework can be used for novel and advanced phenotyping of adult stage zebrafish models of cardiovascular disease, providing a deeper understanding of the mechano-biology of the cardiovascular system of a model organism that is widely used for the study of (the pharmacological treatment of) heritable cardiovascular pathologies.

II. Methods

A. Zebrafish (Danio rerio)

N = 5 male, wild-type, 13 months old adult zebrafish from an AB background were used in this study. Zebrafish experiments were approved by the local ethical committee (ECD 17/78, 2017-09-25) and conducted in strict accordance with the Federation of European Laboratory Animal Science Associations guidelines and recommendations for the care and use of laboratory animals and in compliance with the Directive 2010/63/EU. All applicable international, national and institutional guidelines for the care and use of animals and the conduction of animal experiments were followed.

B. High-frequency ultrasound imaging

Echocardiography measurements were performed with a Vevo 2100 ultrasound machine (FUJIFILM VisualSonics, Toronto, Canada) and MS 700 linear array probe (FUJIFILM VisualSonics, Toronto, Canada). This probe has a frequency range of 30 – 70 MHz and a center frequency of 50 MHz. Tricaine methanesulfonate (MS-222) was used as anesthetic. The fish were first anesthetized in a 1x (0.16 g/L) tricaine solution and a new 0.5x (0.08 g/L) solution was used for anesthesia maintenance during the measurement. Color Doppler and pulsed-wave Doppler measurements of ventricular in- and outflow were recorded with the probe in an abdominocranial short axis configuration at a 45° angle towards the abdominal wall [24]. B-mode images were gathered using longitudinal axis positioning of the probe over the midline of the zebrafish. Before and in between measurements, solutions were placed in a temperature-controlled water bath at constant temperature (28°C). A custom-made holder (3D printed), filled with the 0.5x tricaine solution and including spongy (submersed) clamps, was used to stabilize the zebrafish during echocardiography. Processing of the ultrasound measurements was performed in Vevo LAB (FUJIFILM VisualSonics, Toronto, Canada) by an experienced operator.

C. Specimen preparation for synchrotron imaging

Directly after ultrasound imaging, a lethal dose of tricaine (1 g/L) was used to euthanize the fish. The samples were first fixed in modified Davidson's Fixative overnight, subsequently fixed in 4 % paraformaldehyde and then decalcified in citric acid. All samples were stored in 70 % ethanol (EtOH). On the day of transport, samples were rehydrated by subsequent changes to 50 % EtOH, 25 % EtOH and finally phosphate-buffered saline. As the main cardiovascular structures are located near the zebrafish head, only the most cranial part of the zebrafish was kept.

D. Synchrotron phase-contrast imaging

Propagation-based phase-contrast synchrotron X-ray

imaging was performed at the TOMCAT (X02DA) beamline of the Swiss Light Source (Paul Scherrer Institute in Villigen, Switzerland). Shortly before the scan, samples were immobilized in 1.5 mL Eppendorf tubes filled with agarose gel. All samples were oriented vertically, heads pointing upwards and Eppendorf tubes were fixed onto the robot sample holder using wax. Settings related to the beamline (21.8 keV monochromatic beam energy) and tomography scan (250 mm object-detector distance, 1501 projections, LUAg:CE 20 µm scintillator UPLAPO 4x objective, PCO.Edge 5.5 camera) were optimized during earlier studies on mouse samples [47]. The tomographic reconstruction into image stacks, including phase retrieval, was performed onsite using Paganin's algorithm [48]. Image stacks of 2560 x 2560 pixels and 2160 slices were obtained. At an isotropic voxel size of 1.625 µm³, this corresponds to a field-of-view of 4.16 mm x 4.16 mm (in plane) x 3.51 mm (axial).

E. Segmentation and 3D reconstruction

To reduce computational processing load during the segmentation and 3D reconstruction, images were first converted from 16-bit TIFF to 8-bit JPEG files and the image stacks were downsampled from 2160 to 540 images. This decreased stack sizes from 27.65 GB to 0.47 GB while still allowing accurate 3D reconstructions. The resulting image stacks were semi-automatically segmented in the medical image processing software package Mimics (Materialise, Leuven, Belgium). First, aiming for a mask including both the aortic wall and lumen, a threshold that showed a good trade-off between maximum inclusion of blood spaces and tissue walls of interest and minimum inclusion of neighboring structures was chosen. Then, using the built-in 'multiple slice edit' and 'interpolation' tools, the regions of interest were completely detached from surrounding structures. Holes in this mask were eliminated by using the 'smart fill' tool and on the resulting 3D part, the operations 'wrap' and 'smooth' were applied iteratively. Gill vasculature, sprouting from all pairs of afferent branchial arteries, was not included. A second mask of the lumen only was obtained by eroding the previous mask, hereby taking into account the (major) differences in wall thickness (aorta versus branchial arteries, regions more proximal or distal to the heart). Operations 'wrap' and 'smooth' were applied again on the 3D part. Throughout the whole segmentation process, local irregularities were manually corrected as needed. Both 3D reconstructions (surfaces) were exported to 3-Matic (Materialise, Leuven, Belgium) and uniformly re-meshed into volume meshes to ensure accurate importation in the finite element simulation software. The meshes used for the mesh sensitivity study, including the final mesh, were defined later in the simulation software. There, the afferent branchial arteries were also clipped at approximately 1/3rd of the total branch lengths whereas the beginning of the aorta was clipped about 0.2 mm before the most proximal branching region.

F. Blood flow modeling

Blood was modeled as a Newtonian and incompressible fluid with density 1060 kg/m³ [34]. Lee *et al.* [49] reported a viscosity of 4.17 cP for adult zebrafish but to take the Fåhræus-Lindqvist effect [50], [51] in the small aorta vessel into account, we estimated the viscosity value based on Fig. 2 in the work of Pries *et al.* [51]. A representative diameter of 70 µm returns a viscosity of 2.2 cP, which was used in all simulations. For one sample, blood was also modeled as a power-law fluid defined by the parameters m = 2.2 cP and n = 0.9949 [49] to allow a direct comparison with the baseline results. Laminar blood flow through the ventral aorta was assumed, justified by the low Reynolds number ($Re \approx 15$) that was calculated based on the peak inlet velocity ≈ 300 mm/s, inlet diameter ≈ 0.1 mm, and mentioned viscosity and density values. Body forces, including gravity, were not taken into account. This allows to write the governing equations, i.e., the continuity equation, Eq. 1, and the Navier-Stokes equations, Eq. 2, in following forms:

$$\rho_f \boldsymbol{\nabla} \cdot \vec{V} = 0 \tag{1}$$

$$\rho_f \frac{\partial \vec{V}}{\partial t} + \rho_f (\vec{V} \cdot \boldsymbol{\nabla}) \vec{V} = -\boldsymbol{\nabla} p + \boldsymbol{\nabla} \left(\mu_f \left(\boldsymbol{\nabla} \vec{V} + (\boldsymbol{\nabla} \vec{V})^T \right) \right) \tag{2}$$

where ρ_f is the blood density, $\vec{V}$ the velocity vector, t denotes time, p is the fluid pressure and μ_f the dynamic viscosity.

An animal-specific pulsatile mass flow (kg/s) profile was specified at the inlet. This profile, however, cannot be measured directly in zebrafish as the inlet location of the model (downstream of the bulbus arteriosus, the anatomical structure immediately distal to the ventricle and proximal to our model inlet) is not within the ultrasound acoustic window. The feasible ventricular outflow Doppler flow velocities are not a reasonable approximation since they do not account for the buffering effect of the bulbus arteriosus. We therefore constructed a generic pulsatile flow profile in arbitrary units of one cardiac cycle starting from a measured pulsatile ventral aortic blood flow profile in yellowfin tuna Korsmeyer *et al.* [52] which, a fish species also exhibiting a bulbus arteriosus structure. The waveform was then scaled in magnitude (to mass flow in kg/s) and time using zebrafish sample specific measurements of stroke volume, cardiac cycle time and the ratio of aortic ejection time (AET) per cardiac cycle time. As an example, the applied inlet signal as well as the pulsed wave Doppler recording of ventricular outflow for the same sample are depicted in the right part of Fig. 1. Pressure at the outlets was defined by a purely resistive relationship with the respective flow at that outlet. A total resistance of 2 mmHg·s/mm³ was found assuming a rudimentary mean pressure of 1 mmHg and average flow rate of 0.5 mm³/s. Based on the regular appearance of gill vasculature, fairly equal flow splits were assumed and this was obtained by applying resistances R, $2.5R$, $4R$ and $3.5R$ at the outlets of aortic arches I, II, III and IV, respectively. This is also illustrated in the left part of Fig. 1. R equals 7.74 mmHg·s/mm³ considering the total resistance value and parallel connection of all outlets. In CFD simulations, a no-slip condition was applied at the remaining wall surface.

During the first milliseconds of the simulations, a smoothed step function was used to ramp up the inlet signal from zero. The cycle-to-cycle variations after two cardiac cycles were negligible and the second cycle was post-processed to obtain the results. The CFD Module of finite element software

COMSOL Multiphysics v5.6 (COMSOL Inc., Stockholm, Sweden) was used for all simulations.

G. *Aortic wall and fluid-structure interaction modeling*

In FSI simulations, also the aortic wall and its interaction with the fluid domain was modeled, again using COMSOL multiphysics (CFD Module, Nonlinear Structural Materials Module and Structural Mechanics Module or MEMS Module).

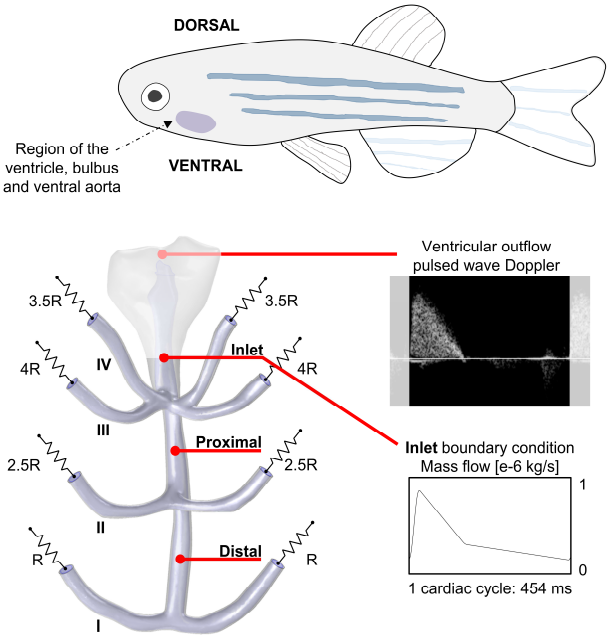

Fig. 1. The location of the ventral aorta is indicated in purple on the zebrafish drawing (top) and a dorsal view of the ventral aorta (and bulbus) is shown below this drawing. Resistive boundary conditions are applied at the eight outlets in the model (same for all samples). Pulsed wave Doppler measurements of ventricular outflow are feasible but clearly differ from the assumed aortic inlet waveform due to the buffering effect of the bulbus arteriosus. The bulbus (shaded) is not explicitly included in the model and the actual inlet location and inlet mass flow boundary condition is depicted. The indicated proximal and distal locations are central locations where flow, pressure and cross section area are evaluated over time. Also pulsed wave velocity (PWV) is calculated at these locations. The aorta geometry and signals of sample #1 are shown.

The FSI problem was solved by using the Arbitrary Lagrangian-Eulerian method. The governing equation to model the deformation of the aortic wall is based on the linear momentum conservation principle, Eq. 3:

$$\rho_s \frac{\partial^2 \vec{U}}{\partial^2 t} - \nabla \bar{\bar{\sigma}} = \rho_s \vec{b} \tag{3}$$

where ρ_s is the density of the vessel wall, $\vec{U}$, the displacement vector, t denotes time, $\bar{\bar{\sigma}}$ is the Cauchy stress tensor and $\vec{b}$ the vector representing body forces applied on the structure. As no (experimental) reference data on the material properties of the aorta in zebrafish was available, a density ρ_s of 1000 kg/m³ and incompressibility were assumed [53] and the fairly simple – for biological tissue common – hyperelastic Neo-Hookean constitutive law was selected. The strain energy density function W can thus be written as:

$$W = \frac{1}{2}\mu_{Lamé}(I_1 - 3) \tag{4}$$

where $\mu_{Lamé}$ is the second Lamé parameter or shear modulus (material constant) and I_1 is the first invariant of the right Cauchy-Green deformation tensor. A shear modulus μ_Lamé of 18 kPa was tuned to obtain plausible diameter (volume) expansions. The percentual diameter (volume) expansions from diastole to systole were assumed to be similar to the data reported in [54]. All inlet and outlet ends of the vessel wall were fully constrained whereas the outer vessel wall surface was free to move. Regarding earlier assumptions about blood flow modeling, the no-slip boundary condition at the wall (CFD simulations) was replaced by a coupled interface between the fluid and vessel walls (FSI simulations) to satisfy the displacement and traction equilibrium. Again, the inlet signal was ramped up from zero and two cardiac cycles were simulated of which only the second cycle was post-processed to obtain the results.

H. *Derived hemodynamic parameters*

Next to basic metrics such as flow, pressure, wall shear stress and principal stress inside the vessel wall, three specific derived hemodynamic parameters, namely time-averaged wall shear stress (TAWSS), oscillatory shear index (OSI) and pulse wave velocity (PWV) were evaluated. TAWSS is defined as follows (Eq. 5):

$$TAWSS = \frac{1}{T}\int_0^T |\overrightarrow{\tau_w}|\, dt \tag{5}$$

where T represents one cardiac cycle, $\overrightarrow{\tau_w}$, the instantaneous WSS vector and t denotes time. The oscillatory shear index reflects the pulsatile aspect of WSS and is calculated according to Eq. 6:

$$OSI = \frac{1}{2}\left(1 - \frac{\left|\frac{1}{T}\int_0^T \overrightarrow{\tau_w}\, dt\right|}{\frac{1}{T}\int_0^T |\overrightarrow{\tau_w}|\, dt}\right). \tag{6}$$

PWV was calculated based on the Bramwell-Hill equation, Eq. 7:

$$PWV = \sqrt{\frac{A_{min}}{\rho_s}\cdot\frac{\Delta P}{\Delta A}} \tag{7}$$

where A_{min} is the minimal luminal area, ρ_s the density of the vessel wall, and ΔP and ΔA denote the difference between maximal and minimal blood pressure and luminal area, respectively, during the cardiac cycle.

I. *Mesh and solver considerations*

For sample #1, a complete mesh sensitivity analysis was conducted with unstructured, corner refined boundary layer meshes of different sizes (Supplementary Figures S1 and S2). Convergence was considered to be achieved for the meshes of 444 716 elements (CFD) and 558 242 elements (FSI). The input parameters of these meshes were then used to define the meshes of all samples, resulting in a similar number of elements for all cases. A direct (PARADISO solver) and fully coupled (Newton method nonlinear solver) scheme was used for all simulations. A relative tolerance of 1e-3 was defined and time steps were determined by the solver but at least one evaluation in every 0.002 s interval was enforced.

III. Results

A. Synchrotron micro-CT based cardiovascular structure and segmentation

All major cardiovascular structures, including the atrium, ventricle, bulbus arteriosus and ventral aorta were clearly visible on the synchrotron images (Fig. 2). Also all four pairs of afferent branchial arteries could be identified. Gill vasculature sprouts in regular fashion and in the end all afferent branchial arteries completely evolve into the gill microcirculation. Blood is then collected in the efferent branchial arteries, located directly next to their afferent counterparts (not included in the 3D reconstruction in panel i of Fig. 2 but visible right above the afferent branchial arteries in panels a-e of Fig. 2). For some samples, the efferent branchial arteries could be tracked until the merge with the dorsal aorta (not visible in Fig. 2).

Representative results for the segmentation of the aortic wall and lumen are shown in Fig. 3. For CFD simulations, only the

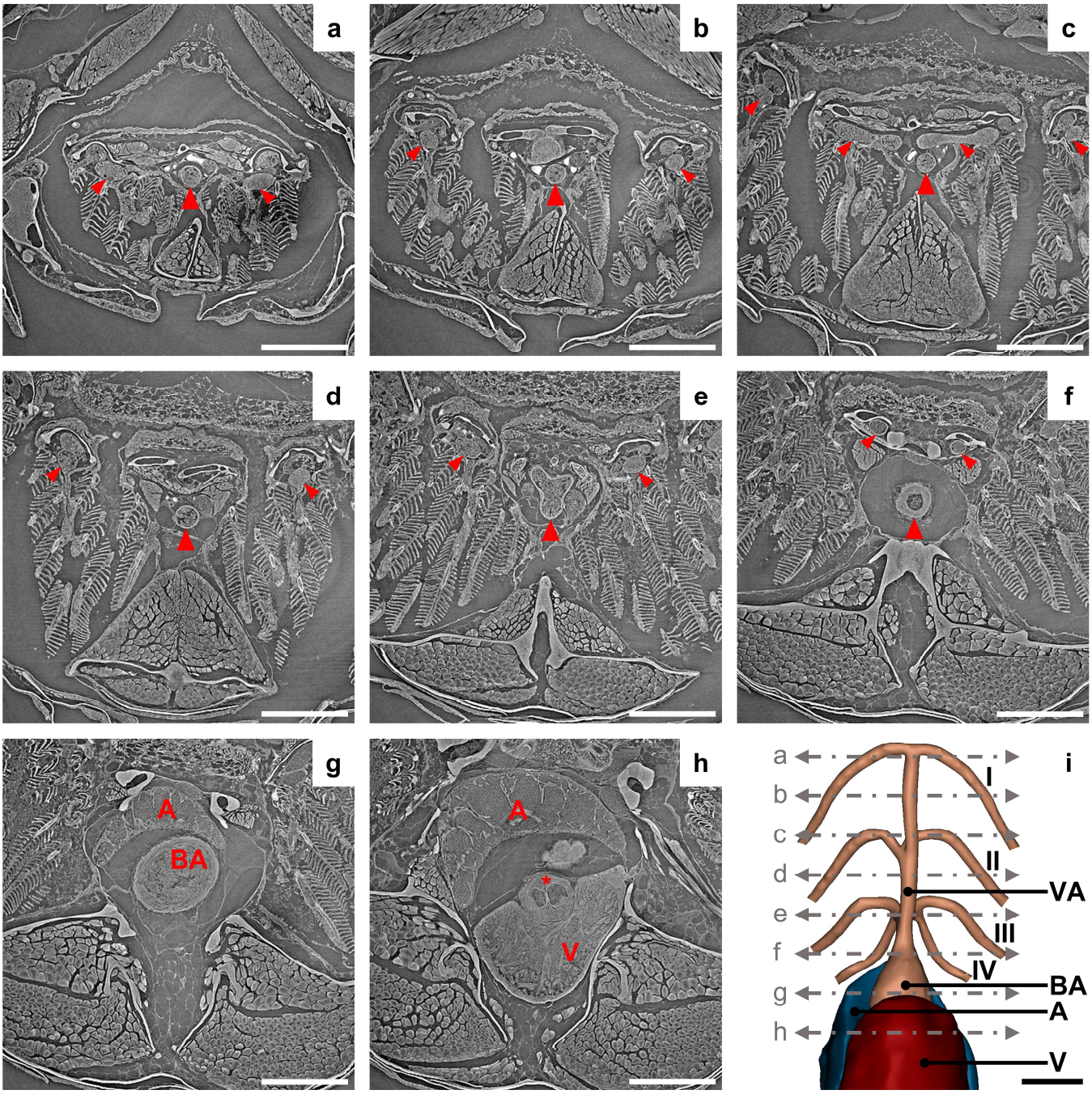

Fig. 2. Synchrotron imaging can be used to visualize and 3D reconstruct all major cardiovascular structures in adult zebrafish. Panels a-h show equally spaced (325 µm) axial cross sections of the ventral aorta (large arrowheads), afferent branchial arteries (small arrowheads), bulbus arteriosus, atrium and ventricle. The asterisk in panel h indicates the aortic valve region. Panel i shows the resulting 3D reconstruction with indications of the locations of all cross sections. The ventricle, atrium and all four pairs of afferent branchial arteries (named I-IV) are clipped in the 3D visualization. VA: ventral aorta, BA: bulbus arteriosus, A: atrium, V: ventricle. Scale bars: 500 µm.

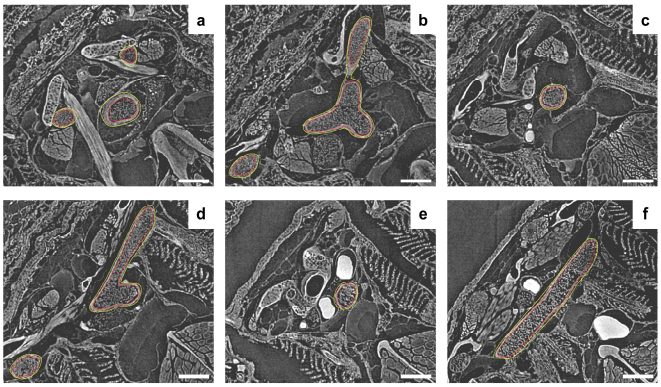

Fig. 3. Semi-automatic segmentation of the aortic vessel wall and lumen. The outer boundary of the vessel wall is traced in yellow whereas the inner boundary of the vessel wall, which is also the outer boundary of the blood lumen, is traced in red. Six different cross sections of the same sample are shown as a representative example. Panels a-f show cross sections of the ventral aorta in proximal to distal order. Panel a shows a cross section around the inlet location (end of the transition from the bulbus arteriosus to the ventral aorta which is before the first branching region). Panel b shows a cross section near the first branching region (branchial arteries III and IV). Panel d shows the middle branching region (branchial arteries II) whereas panel f shows the last branching region (branchial arteries I). Panels c and e show the ventral aorta in non-branching regions. Scale bars: 100 µm.

lumen boundaries are used (red) whereas for FSI simulations both the lumen boundaries and outer vessel wall boundaries (yellow) are used. This way, the CFD geometry and the fluid domain in the FSI geometry at time step zero are identical.

B. *Measurements of cardiovascular structure and function*

Table I provides a quantitative summary of both *ex vivo* structural data and *in vivo* functional data of the five samples. Structural parameters (row 3-6) result from the synchrotron-based segmentations and 3D reconstructions. Functional parameters (row 7-11) result from high-frequency B-mode echocardiography measurements.

TABLE I
QUANTITATIVE SUMMARY OF SYNCHROTRON-BASED STRUCTURAL CARDIOVASCULAR PARAMETERS AND ECHOCARDIOGRAPHY-BASED FUNCTIONAL CARDIOVASCULAR PARAMETERS

	#1	#2	#3	#4	#5
Body weight [mg]	216	290	191	187	230
Length [mm]	28	32	29	27	30
Aorta lumen volume [10^{-3} mm³]	25	51	36	34	33
Aorta wall volume [10^{-3} mm³]	15	22	19	16	15
Avg. wall thickness [µm]	9.14	9.53	8.34	11.65	8.89
Aorta lumen inlet [10^{-3} mm²]	7.11	6.29	5.81	7.28	7.06
Stroke volume [µL]	0.15	0.48	0.15	0.29	0.26
Total (cardiac) cycle [ms]	454	440	428	390	444
Heart rate [bpm]	132	136	140	154	135
Cardiac output [µL/min]	19.73	65.91	20.51	44.09	35.33
Ratio AET/total cycle [-]	0.34	0.34	0.33	0.34	0.29

The reported heart rate corresponds to the (B-mode based) cardiac cycle time measurement and cardiac output was calculated from the stroke volume and heart rate values. Body weight and length (row 1-2) were measured directly after the echocardiography experiments.

C. *Hemodynamics of the aorta*

For the sake of clarity, this results section focusses on data retrieved from the FSI simulations. The assessment of the CFD data and the similarities and differences with the FSI data are considered in the discussion and through supplementary materials.

Pressure, blood flow and pulse wave velocity

Pressure (mmHg), blood flow (mm³/s) and luminal area (mm²) were evaluated around the middle of both straight segments of the ventral aorta (called 'proximal' and 'distal' location as displayed in Fig. 1). Fig. 4 depicts the time profiles of these metrics for sample #1 at both locations. At the same locations, pulse wave velocity (PWV) was evaluated with the Bramwell-Hill relationship (Eq. 7). A PWV of 1.74 – 2.25 m/s (observed range considering all 5 samples) was obtained at the proximal location whereas a PWV of 1.89 – 2.09 m/s was obtained downstream at the distal location. For each sample, the time-averaged mass flow splits (compared to the inlet mass flow) of all four pairs of branchial arteries fell within the 20 – 31 % range. For sample #1, a FSI animation of the flow throughout the complete cardiac cycle is added as Supplementary Video A1. Arrows point towards the local flow direction and both the color and length (on a logarithmic scale) of the arrows represent velocity magnitude. CFD time profiles equivalent to the FSI results presented in Fig. 4 are reported in Supplementary Figure S3.

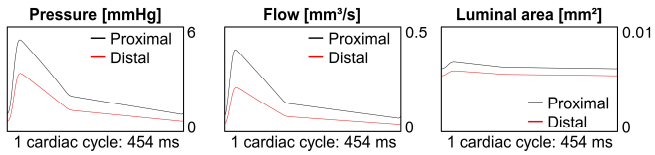

Fig. 4. Time profiles of pressure, blood flow and luminal area for sample #1 in FSI simulations. Black lines depict the profiles at the proximal location whereas red lines are evaluated at the distal location. In each panel, one complete cardiac cycle is shown.

Wall shear stress

TAWSS is displayed in Fig. 5. Surface-averaged TAWSS values of 2.52 – 5.49 Pa were obtained. A clear visualization of lowest TAWSS regions is depicted at the bottom of Fig. 5 by using a different color scale. The 5th and 10th percentiles of TAWSS ranged between 1.44 – 2.91 Pa and 1.58 – 3.24 Pa, respectively. For sample #1, a FSI (and CFD) animation of WSS magnitude throughout the complete cardiac cycle is added as Supplementary Video A2. Surface-averaged WSS at systolic peak was 5.71 – 11.47 Pa. In Fig. 6, oscillatory shear is presented by plotting the OSI and peak OSI values of 0.007 – 0.059 were found. A comparison of the WSS at systolic peak for the Newtonian versus the power-law fluid model returned average and maximum differences of 3.32 % and 5.45 %, respectively.

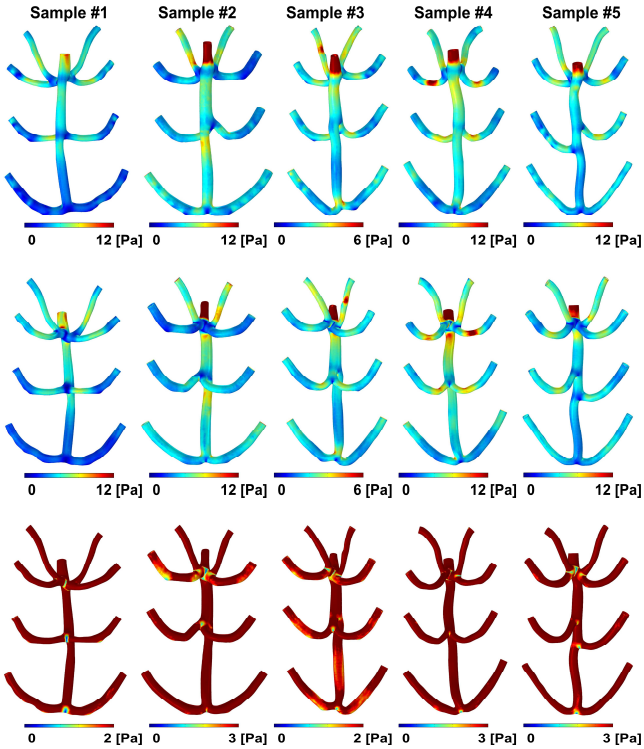

Fig. 5. Time-averaged wall shear stress (TAWSS) in FSI simulations. For each sample, two views are provided (a view of the ventral side on the top row and a view of the dorsal side on the middle row). At the bottom, the middle row is replotted on a different color scale to get a more clear visualization of lowest TAWSS regions. Note the different color scale for sample #3 in all rows as well as for sample #1 in the bottom row.

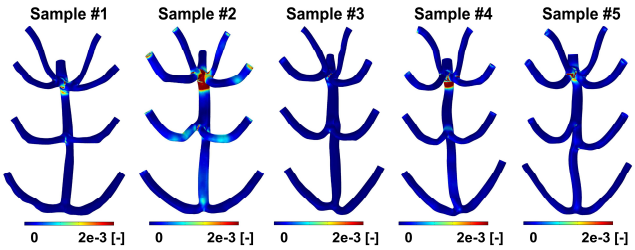

Fig. 6. Oscillatory Shear Index (OSI) in FSI simulations. The OSI can take values between 0 and 0.5 corresponding to a uni-directional flow and reversing flow with no mean direction, respectively.

Shear stress related CFD results are reported in Supplementary Figures S4 and S5.

Stress inside the vessel wall

First principal stress, evaluated at the inner vessel wall surface at systolic peak, is shown in Fig. 7. Peak values of 25 – 88 kPa were obtained. For sample #1, an animation of first principal stress at the inner and outer vessel wall surfaces throughout the complete cardiac cycle is added as Supplementary Video A3.

IV. Discussion

In this study we used *ex vivo* synchrotron imaging and *in vivo* high-frequency echocardiography to set up unprecedented CFD and FSI finite element models of the ventral aorta in adult zebrafish. Relevant hemodynamic parameters such as flow,

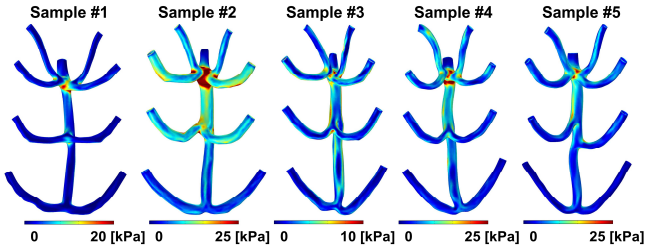

Fig. 7. First principal stress at systolic peak in FSI simulations. The inner surface of the vessel wall is visualized. Note the different color scale for samples #1 and #3.

pressure, wall shear stress related metrics and first principal stress in the vessel wall are evaluated.

The general image quality of our synchrotron experiments agrees with other studies that applied synchrotron imaging to juvenile and adult zebrafish [43]-[46]. None of the other studies explicitly focused on the cardiovascular structures and therefore the 3D reconstructions of the aorta and aortic arches presented here provide a novel, useful anatomical reference. Aortic arches II of sample #5 connect to the aorta at different (asymmetric) locations. Apart from this remarkable difference, the geometry of the ventral aorta segments and their branching points is similar. A visual evaluation of the segmentation (Fig. 3) shows a good overall accuracy of the semi-automatic segmentation approach. The thickness of the vessel wall was slightly overestimated in some regions and this was tolerated to allow a semi-automatic rather than a fully manual segmentation. Moreover, the stiffness of the aorta greatly influences the mechanical behavior and the slight overestimation of wall thickness in certain regions is likely to be negligible compared to the simplifications and assumptions regarding material model and constants.

The distribution in the body weights of the zebrafish used for synchrotron imaging reflects the natural biological variability. The echocardiography-based measurements of stroke volume (0.15 – 0.48 µL) and heart rate (133 – 154 bpm) fall within the range reported in the literature [26]. Age and anesthesia (time) also affect these values. Variability in simulated hemodynamic results is present as well but the overall patterns of simulated hemodynamic results agree well between different animals as can be appreciated from Fig. 5, Fig. 6 and Fig. 7. Note that for some samples, the color scaling was altered to present this similarity more clearly.

First, FSI fluid dynamics results are discussed. Although a direct quantitative scaling of zebrafish to human flow field parameters is difficult, we still compare the results with human and mice data to put the observed order of magnitudes in context. Simulated mean pressures at the distal location (1.25 – 3.03 mmHg) agree with the mean pressure reported by Hu *et al.* (≈ 1.25 mmHg) [41] whereas the simulated mean pressures at the proximal location (1.65 – 4.08 mmHg) are slightly higher. Obtained peak pressures at the proximal (3.91 – 8.76 mmHg) and distal (3.00 – 6.79 mmHg) locations are higher but still in the same order of magnitude compared to the ventral aortic peak pressures reported by Hu *et al.* (≈ 2.16 mmHg) [41]. Experimental blood pressure measurements in zebrafish are challenging because of the small vessel and chamber

dimensions (long axis ventricle ≈ 1 mm, inlet diameter ventral aorta ≈ 0.1 mm) and the difficulty of applying a pressure servo null system invasively at these sites. The report by Hu *et al.* in 3 month old zebrafish is the only reference on arterial blood pressure in adult zebrafish that we could identify. The same group showed that ventricular systolic and diastolic as well as aortic peak pressures increase geometrically with age during development [55] and later measurements by Kopp *et al.* [56] in 2.5-3 dpf embryos are in line with their reported values. Recently, much higher peak ventricular pressures in 5 dpf zebrafish were reported [57] whereas stroke volumes were comparable to the measurements of [56] and [55]. This emphasizes the need for both more longitudinal (throughout development until late adulthood) and better documented (mentioning the precise measurement location in the ventral aorta) pressure measurements in zebrafish. Overall, ventral aortic pressures resulting from our model seem plausible and agree with the reported order of magnitudes.

The evaluated wall shear stress related metrics (WSS, TAWSS and OSI) revealed consistent patterns for all samples. TAWSS is lowest near the dorsal side of the branching regions (not considering the aortic arches). Throughout the complete cardiac cycle, the instantaneous WSS pattern is very similar to the TAWSS pattern and only differs in magnitude. WSS magnitudes at systolic peak are roughly double the TAWSS values. Simulated WSS magnitudes are higher compared to adult mice and humans and more similar to WSS magnitudes observed in prenatal mice [58]. Due to the different aorta geometry in zebrafish compared to mammals, a comparison of overall WSS and TAWSS patterns between species is difficult. The (branched) zebrafish aorta geometry actually resembles – to some extent – the aorta and aortic arches of the chick embryo and also WSS magnitudes of the same order of magnitude are observed [59]. OSI patterns show that the dorsal sides of the most proximal branching regions are also the locations with highest oscillatory shear. Some variability is present in terms of the magnitude and size of this most proximal peak OSI region (especially for samples #2 and #4) but the general pattern is consistent. Highest observed oscillatory shear regions thus largely coincide with lowest wall shear stress regions. OSI magnitudes are very low compared to, e.g., mice [60] and humans [61]. The very low oscillatory shear may seem counterintuitive due to the presence of several branching regions, but can be explained by the very low peak Reynolds number ($Re \approx 15$) and associated highly laminar flow behavior. Peak Reynolds numbers in the aorta of adult mice (≈ 350) and humans (≈ 7500) are considerably higher which leads to more disturbed flow regions.

For four out of five cases, pulse wave velocity was higher at the distal measurement location compared to the proximal measurement location. The values of approximately 2 m/s are of the same order of magnitude as PWV in the healthy human and mouse aorta.

In our simulations, highest first principal stress locations in the vessel wall are observed near the most proximal branching region. Around and in between the connections of aortic arches III and IV, several stress hotspots were found. First principal stress was also relatively high near the middle branching region. The location of peak first principal stress around the most proximal branching region is not totally unexpected, but it is interesting to see such distinct and similar first principal stress hotspots and patterns in all samples. Note that some similarities can be observed between the overall patterns of low TAWSS (Fig. 5 bottom row), OSI (Fig. 6) and first principal stress (Fig. 7). The highest values of first principal stress values are one order of magnitude below the values reported in mice [29] and humans [62].

Comparing the flow results of FSI and CFD simulations, most key findings agree with literature. Peak pressures are higher throughout the model in CFD simulations because of the rigid lumen walls (Supplementary Figure S3). Also (peak) instantaneous WSS and TAWSS are slightly higher in CFD simulations whereas the overall patterns are almost identical (Supplementary Video A2 and Fig. 5 versus Supplementary Figure S4). Several groups reported that OSI patterns and magnitude in both mice [63] and humans [61] can differ considerably in CFD and FSI simulations. No clear difference in the OSI patterns of CFD and FSI simulations was observed, but OSI magnitudes were about one order of magnitude lower in CFD simulations compared to FSI simulations (Fig. 6 versus Supplementary Figure S5). Overall, CFD simulations can give accurate qualitative information on the fluid dynamics. Whereas FSI magnitudes of all metrics are likely to be more accurate, the increased computational effort and uncertainty of several model parameters (inlet and outlet boundary conditions, stiffness aorta vessel…) are arguments in favor of CFD simulations if only the mentioned flow related parameters are important. FSI simulations can still be necessary depending on the application, e.g., to quantify first principal stress inside the vessel wall or to study disease conditions that affect vascular wall properties.

Below, we discuss certain choices and assumptions and also address the limitations of the current models and modeling approach. Synchrotron micro-CT imaging was used in order to provide an optimal combination of resolution and soft tissue contrast. Vascular corrosion casting could allow to use traditional micro-CT instead of synchrotron radiation while a high level of detail showing, e.g., the trabeculation of the ventricle [64], can still be obtained. Corrosion casting however cannot be used to reconstruct the vessel wall geometry as all tissue information is lost. On the other hand, corrosion casting could provide fast segmentations of the CFD geometries and the obtained 3D reconstructions may actually be a (slightly) better representation of the *in vivo* intraluminal dimensions. The vascular corrosion casting workflow [64] as well as our presented synchrotron imaging workflow are intrinsically *ex vivo* procedures. Magnetic resonance imaging (MRI) seems a promising option to obtain *in vivo* three-dimensional geometries but remains very challenging in zebrafish. Only for larger structures like the atrium, ventricle and bulbus arteriosus, the use of MRI was successfully reported [12], [65]. At this point, MRI nor 4D high-frequency echocardiography provides sufficient resolution to evaluate the deformation of the ventral aorta and aortic arches in adult zebrafish. If imaging techniques

become available that allow accurate 3D reconstructions of *in vivo* measurements of the aorta structure, simulations including pre-stress can be considered. Customized high-frequency ultrasound set ups can be used to push resolution limits as recently reported [66], [67] but require specialized material and staff. Pulsed wave Doppler or M-mode measurements in the ventral aorta could become feasible in the near future and can then be used to construct the inlet signal and to provide *in vivo* validation of simulation results.

A reduced zebrafish blood viscosity was used because the Fåhræus-Lindqvist effect may play a prominent role. In small arteries (D < 0.3 mm), red blood cells tend to migrate to center of small vessels and effective viscosity near the wall is more similar to the viscosity of plasma [50], [51]. Although often accepted for mice and humans, the assumption to model blood as a Newtonian fluid is not trivial for zebrafish. In (adult) mice and humans, the compressible effect of individual red blood cells is mostly negligible when looking at the whole blood suspension as vessel diameters are usually large compared to blood cell diameters. However, for the zebrafish circulation, red blood cell diameters tend to approach (some) vessel diameters which could make blood viscosity more shear rate dependent and therefore non constant. Two arguments make the constant viscosity assumption (Newtonian fluid) in our models still reasonable: (i) only large vessels of the zebrafish circulation were included in our simulations and (ii) Lee *et al.* [49] demonstrated that blood viscosity in adult zebrafish stays fairly constant over the vast majority of shear rates encountered during the simulations. This is also reflected by the small WSS differences (at systolic peak) for the Newtonian and power-law fluid model.

Explicit validation of several assumptions is difficult at this point, including viscosity modeling, outlet flow splits and material model and constants of the vessel wall. If the modeling workflow is consistently used, e.g., to compare different pathological conditions, valuable results can be obtained nonetheless. In future work, several zebrafish models of heritable thoracic aortic disease will be compared with the presented wild-type baseline data. In addition, other cardiovascular structures such as the bulbus arteriosus will be modeled explicitly. Ongoing advances in zebrafish echocardiography and MRI will also provide more *in vivo* validation options.

V. Conclusion

In summary, we have shown that modeling the cardiovascular fluid dynamics and biomechanics in adult zebrafish is feasible. Synchrotron imaging can provide accurate three-dimensional reconstructions of the main cardiovascular structures, which is complemented by high-frequency ultrasound measurements to provide additional information on *in vivo* blood flow characteristics. This study provides the first reference values for multiple key biomechanical stimuli in wild-type adult zebrafish, including wall shear stress and first principal stress. The presented framework can be used for advanced cardiovascular phenotyping of adult genetically engineered zebrafish models of cardiovascular disease, showing disruptions of the normal mechano-biology and homeostasis. This way, biomechanical phenotyping in zebrafish is no longer limited to the developing stages, as earlier reported, and also progressive or late onset conditions and phenotypes can be investigated. By providing a pipeline for image-based animal-specific computational biomechanical models in zebrafish, a model organism that is increasingly used for the study of heritable cardiovascular pathophysiology, this study contributes to a more comprehensive understanding of the role of altered biomechanics and hemodynamics in cardiovascular pathologies.

Acknowledgment

We acknowledge the Paul Scherrer Institute, Villigen, Switzerland for providing synchrotron radiation beamtime at the TOMCAT beamline of the Swiss Light Source. We also thank Gerlinde Logghe and Regina Le Roux for their help during the synchrotron experiment.

References

[1] G. J. Lieschke and P. D. Currie, "Animal models of human disease: Zebrafish swim into view," *Nat. Rev. Genet.*, vol. 8, pp. 353-367, 2007.
[2] A. Asnani and R. T. Peterson, "The zebrafish as a tool to identify novel therapies for human cardiovascular disease," *Dis. Model. Mech.*, vol. 7, pp. 763-767, Jul. 2014.
[3] G. Bowley *et al.*, "Zebrafish as a tractable model of human cardiovascular disease," *Br. J. Pharmacol.*, vol. 179, pp. 900-917, 2022.
[4] T. Dahme *et al.*, "Fishing for the genetic basis of cardiovascular disease," *Dis. Model. Mech.*, vol. 2, pp. 18-22, Jan. 2009.
[5] C. A. MacRae and R. T. Peterson, "Zebrafish as tools for drug discovery," *Nat. Rev. Drug Discov.*, vol. 14, pp. 721-731, Sep. 2015.
[6] Y Zhao *et al.*, "Screening drugs for myocardial disease in vivo with zebrafish: an expert update," *Expert Opin. Drug Discov.*, vol. 14, pp. 343-353, Apr. 2019.
[7] J. Bakkers, "Zebrafish as a model to study cardiac development and human cardiac disease," *Cardiovasc. Res.*, vol. 91, pp. 279-288, Jul. 2011.
[8] K. M. Ross Stewart *et al.*, "Hooked on heart regeneration: the zebrafish guide to recovery," *Cardiovasc. Res.*, vol. 118, pp. 1167-1179, 2022.
[9] B. M. Weinstein *et al.*, "Gridlock, a localized heritable vascular patterning defect in the zebrafish," *Nat. Med.*, vol. 1, pp. 1143-1147, Nov. 1995.
[10] D. C. Guo *et al.*, "MAT2A mutations predispose individuals to thoracic aortic aneurysms," *Am. J. Hum. Genet.*, vol. 96, pp. 170-177, Jan. 2015.
[11] G. L. M. Boezio *et al.,* "Endothelial TGF-β signaling instructs smooth muscle cell development in the cardiac outflow tract," *Elife,* vol. 9, Sep. 2020, Art. no. e57603.
[12] A. Bensimon-Brito and G. L. M. Boezio *et al.*, "Integration of multiple imaging platforms to uncover cardiovascular defects in adult zebrafish," *Cardiovasc. Res.*, Oct. 2021, Art. no. cvab310.
[13] P. Y. Sips *et al.*, "Characterizing the cardiovascular phenotype of a new zebrafish model of Marfan syndrome," *Eur. Heart J.*, vol. 42, no. Supplement 1, Oct. 2021, Art. no. ehab724.3379.
[14] A. Prendergast *et al.*, "Phenotyping zebrafish mutant models to assess candidate genes associated with aortic aneurysm," *Genes (Basel)*, vol. 13, no. 1, Jan. 2022, Art. no. 123.
[15] M. Abrial *et al.*, "Latent TGFβ-binding proteins 1 and 3 protect the larval zebrafish outflow tract from aneurysmal dilatation," *Dis. Model. Mech.*, vol. 15, Mar 2022, Art. no. dmm046979.
[16] N. D. Lawson and B. M. Weinstein, "In vivo imaging of embryonic vascular development using transgenic zebrafish," *Dev. Biol.*, vol. 248, pp. 307-318, Aug. 2002.
[17] J. T. Shin *et al.*, "High-resolution cardiovascular function confirms functional orthology of myocardial contractility pathways in zebrafish," *Physiol. Genomics.*, vol. 42,, no. 2, pp. 300-309, Jul. 2010.
[18] W. Y. Hwang *et al.*, "Efficient genome editing in zebrafish using a CRISPR-Cas system," *Nat. Biotechnol.*, vol. 31, no. 3, pp. 227-229, Mar. 2013.

[19] Y. Ding *et al*., "Multiscale light-sheet for rapid imaging of cardiopulmonary system," *JCI Insight*, vol. 3, no. 16, Aug. 2018, Art. no. e121396.

[20] Z. Wang *et al*., "A hybrid of light-field and light-sheet imaging to study myocardial function and intracardiac blood flow during zebrafish development," *PLoS Comput. Biol.*, vol. 17, no. 7, Jul. 2021, Art. no. e1009175.

[21] R. M. White *et al.*, "Transparent adult zebrafish as a tool for in vivo transplantation analysis," *Cell Stem Cell*, vol. 2, no. 2, pp. 183-189, Feb. 2008.

[22] D. Castranova *et al.*, "Long-term imaging of living adult zebrafish," *Development*, vol. 149, no. 4, Feb. 2022, Art. no. dev199667.

[23] L. Sun *et al.*, "In vivo cardiac imaging of adult zebrafish using high frequency ultrasound (45-75 MHz)," *Ultrasound Med. Biol.*, vol. 34, no. 1, pp. 31-39, Jan. 2008.

[24] S. J. Hein *et al*., "Advanced echocardiography in adult zebrafish reveals delayed recovery of heart function after myocardial cryoinjury," *PLoS One*, vol. 10, no. 4, Apr. 2015, Art. no. e0122665.

[25] C. C. Huang CC *et al.*, "High-resolution tissue doppler imaging of the zebrafish heart during its regeneration," Zebrafish, vol. 12, no. 1, pp. 48-57, Feb. 2015.

[26] L. W. Wang *et al.*, "Standardized echocardiographic assessment of cardiac function in normal adult zebrafish and heart disease models," *Dis. Model. Mech.*, vol. 10, no. 1, pp. 63–76, Jan. 2017.

[27] D. Lu and G. S. Kassab, "Role of shear stress and stretch in vascular mechanobiology," *J. R. Soc. Interface*, vol. 8, no. 63, pp. 1379-1385, Oct. 2011.

[28] J. M. Dolan *et al*., "High wall shear stress and spatial gradients in vascular pathology: a review," *Ann. Biomed. Eng.*, vol. 41, no. 7, pp. 1411-1427, Jul. 2013.

[29] B. Trachet *et al.*, "An animal-specific FSI model of the abdominal aorta in anesthetized mice," *Ann. Biomed. Eng*., vol. 43, no. 6, pp. 1298-1309, Jun. 2015.

[30] J. Lee *et al.*, "Moving domain computational fluid dynamics to interface with an embryonic model of cardiac morphogenesis," *PLoS One*, vol. 8, no. 8, Aug. 2013, Art. no. e72924.

[31] R. A. Jamison *et al.*, "In vivo wall shear measurements within the developing zebrafish heart," *PLoS* One, vol. 8, no. 10, Oct. 2013, Art. no. e75722.

[32] F. Boselli and J. Vermot, "Live imaging and modeling for shear stress quantification in the embryonic zebrafish heart," *Methods*, vol. 94, pp. 129-134, Feb. 2016.

[33] H. C. Yalcin *et al.*, "Heart function and hemodynamic analysis for zebrafish embryos," *Dev. Dyn.*, vol. 246, no. 11, pp. 868-880, 2017.

[34] V. Vedula *et al.*, "A method to quantify mechanobiologic forces during zebrafish cardiac development using 4-D light sheet imaging and computational modeling," *PLoS Comput. Biol.*, vol. 13, no. 10, Oct. 2017, Art. no. e1005828.

[35] J. J. Hsu *et al.*, "Contractile and hemodynamic forces coordinate Notch1b-mediated outflow tract valve formation," *JCI Insight*, vol. 4, no. 10, May 2019, Art. no. e124460.

[36] Y. Y. Foo *et al*., "4D modelling of fluid mechanics in the zebrafish embryonic heart," *Biomech. Model. Mechanobiol.*, vol. 19, no. 1, pp. 221-232, Feb. 2020.

[37] H. E. Salman and Y. C. Yalcin, "Computational modeling of blood flow hemodynamics for biomechanical investigation of cardiac development and disease," *J. Cardiovasc. Dev. Dis*., vol. 8, no. 2, 2021, Art. no. 14.

[38] S. J. Lee *et al.*, "Association of early atherosclerosis with vascular wall shear stress in hypercholesterolemic zebrafish," *PLoS One*, vol. 10, no. 11, Nov. 2015, Art. no. e0142945.

[39] W. Choi *et al.*, "Variation in wall shear stress in channel networks of zebrafish models," *J. R. Soc. Interface*, vol. 14, no. 127, Feb. 2017, Art. no. 20160900.

[40] M. Roustaei *et al.*, "Computational simulations of the 4D micro-circulatory network in zebrafish tail amputation and regeneration," *J. R. Soc. Interface*, vol. 19, no. 187, Feb. 2022, Art. no. 20210898.

[41] N. Hu *et al.*, "Cardiac morphology and blood pressure in the adult zebrafish," *Anat. Rec*., vol. 264, no. 1, pp. 1-12, Sep. 2001.

[42] A.L. Menke *et al*., "Normal anatomy and histology of the adult zebrafish," *Toxicol. Pathol*., vol. 39, no. 5, pp. 759-775, Aug. 2011.

[43] K. C. Cheng *et al.*, "Whole-animal imaging, gene function, and the Zebrafish Phenome Project," *Curr. Opin. Genet. Dev*., vol. 21, no. 5, pp. 620-629, Oct. 2011.

[44] E. Seo *et al.*, "Whole-body imaging of a hypercholesterolemic female zebrafish by using synchrotron X-ray micro-CT," *Zebrafish*, vol. 12, no. 1, pp. 11-20, Feb. 2015.

[45] V. Weinhardt *et al.*, "Quantitative morphometric analysis of adult teleost fish by X-ray computed tomography," *Sci. Rep.*, vol. 8, Nov. 2018, Art. no. 16531.

[46] Y. Ding *et al*., "Computational 3d histological phenotyping of whole zebrafish by x-ray histotomography," *Elife*, vol. 8, May 2019, Art. no. e44898.

[47] G. Logghe *et al.*, "Propagation-based phase-contrast synchrotron imaging of aortic dissection in mice: from individual elastic lamella to 3D analysis," *Sci. Rep.*, vol. 8, Feb. 2018, Art. no. 2223.

[48] D. Paganin *et al*., "Simultaneous phase and amplitude extraction from a single defocused image of a homogeneous object," *J. Microsc.*, vol. 206, no. 1, pp. 33-40, Apr. 2002.

[49] J. Lee *et al.*, "A rapid capillary-pressure driven micro-channel to demonstrate Newtonian fluid behavior of zebrafish blood at high shear rates," *Sci. Rep*., vol. 7, May 2017, Art. no. 1980.

[50] R. Fåhræus and T. Lindqvist, "The viscosity of the blood in narrow capillary tubes," *Am. J. Physiol. – Legacy Content*, vol. 96, no. 3, pp. 562-568, Mar. 1931.

[51] A. R. Pries *et al.*, "Blood viscosity in tube flow: Dependence on diameter and hematocrit," *Am. J. Physiol. – Hear. Circ. Physiol.*, vol. 263, no. 32, pp. 1770-1778, Dec. 1992.

[52] K. E. Korsmeyer *et al.*, "Heart rate and stroke volume contributions to cardiac output in swimming yellowfin tuna: Response to exercise and temperature," *J. Exp. Biol.*, vol. 200, no. 14, pp. 1975-1986, Jul. 1997.

[53] C. W. Ong *et al.*, "Pulsatile flow investigation in development of thoracic aortic aneurysm: an in-vitro validated fluid structure interaction analysis," *J. Appl. Fluid Mech.*, vol. 12, no. 6, pp. 1855-1872, 2019.

[54] M. Braun *et al*., "Form and function of the bulbus arteriosus in yellowfin tuna (Thunnus albacares), bigeye tuna (Thunnus obesus) and blue marlin (Makaira nigricans): dynamic properties," *J. Exp. Biol.*, vol. 206, no. 19, pp. 3327-3335, Jun. 2003.

[55] N. Hu *et al.*, "Structure and function of the developing zebrafish heart," *Anat. Rec*., vol. 260, no. 2, pp. 148-157, Oct. 2000.

[56] R. Kopp *et al.*, "Cardiac performance in the zebrafish breakdance mutant," *J. Exp. Biol*., vol. 208, no. 11, pp. 2123-2134, Jun. 2005.

[57] N. Salehin *et al.*, "Assessing pressure–volume relationship in developing heart of zebrafish in-vivo," *Ann. Biomed. Eng.*, vol. 49, no. 9, pp. 2080-2094, Sep. 2021.

[58] C. H. Yap *et al.*, "Characterizaton of the vessel geometry, flow mechanics and wall shear stress in the great arteries of wildtype prenatal mouse," *PLoS One*, vol. 9, no. 1, Jan. 2014, Art. no. e86878.

[59] Y. Wang *et al*., "Aortic arch morphogenesis and flow modeling in the chick embryo," *Ann. Biomed. Eng.*, vol. 37, no. 6, pp. 1069-1081, 2009.

[60] B. Trachet *et al*., "Impact of simplified boundary conditions and aortic arch inclusion on CFD simulations in the mouse aorta: a comparison with mouse-specific reference data," *J. Biomech. Eng*., vol. 133, no. 12, Dec. 2011, Art. no. 121006.

[61] M. Alimohammadi *et al.*, "Aortic dissection simulation models for clinical support: fluid-structure interaction vs. rigid wall models," *Biomed. Eng. Online*, vol. 14, Apr. 2015, Art. no. 34.

[62] S. R. de Galarreta *et al.*, "The relationship between surface curvature and abdominal aortic aneurysm wall stress," *J. Biomech. Eng.*, vol. 139, no. 8, Aug. 2017.

[63] D. De Wilde *et al.*, "The influence of anesthesia and fluid–structure interaction on simulated shear stress patterns in the carotid bifurcation of mice," *J. Biomech.*, vol. 49, no. 13, pp. 2741-2747, Sep. 2016.

[64] W. De Spiegelaere *et al.*, "Corrosion casting of the cardiovascular structure in adult zebrafish for analysis by scanning electron microscopy and X-ray microtomography," *Anat. Histol. Embryol*., vol. 49, no. 5, pp. 635-642, Sep. 2020.

[65] J. Koth *et al.*, "High-resolution magnetic resonance imaging of the regenerating adult zebrafish heart," *Sci. Rep.*, vol. 7, Jun. 2017, Art. no. 2917.

[66] C. C. Chang *et al.*, "In vivo visualization of vasculature in adult zebrafish by using high-frequency ultrafast ultrasound imaging," *IEEE Trans. Biomed. Eng.*, vol. 66, no. 6, pp. 1742-1751, Jun. 2019.

[67] C. Ho-Chiang *et al.*, "High-frequency ultrasound deformation imaging for adult zebrafish during heart regeneration," *Quant. Imaging Med. Surg.*, vol. 10, no. 1, pp. 66-75, Jan. 2020.